*Inorg. Chem.* **2002**, *41*, 2124–2133

# Ligand Influences on Copper Molybdate Networks: The Structures and Magnetism of $[Cu(3,4'\text{-bpy})MoO_4]$, $[Cu(3,3'\text{-bpy})_{0.5}MoO_4]$, and $[Cu(4,4'\text{-bpy})_{0.5}MoO_4]\cdot 1.5H_2O$

**Randy S. Rarig, Jr.,[†] Robert Lam,[‡] Peter Y. Zavalij,[§] J. Katana Ngala,[§] Robert L. LaDuca, Jr.,[||] John E. Greedan,*[,‡] and Jon Zubieta*[,†]**

*Department of Chemistry, Syracuse University, Syracuse, New York 13244, Department of Chemistry, McMaster University, Hamilton, Ontario, Canada L8S 4M1, Department of Chemistry and Physics, King's College, Wilkes-Barre, Pennsylvania 18711, and Chemistry Department and Materials Research Center, State University of New York at Binghamton, Binghamton, New York 13902*

Received November 12, 2001

The reactions of a Cu(II) salt, $MoO_3$, and the appropriate bipyridine ligand yield a series of bimetallic oxides, $[Cu(3,4'\text{-bpy})MoO_4]$ (**1**), $[Cu(3,3'\text{-bpy})_{0.5}MoO_4]$ (**2**), and $[Cu(4,4'\text{-bpy})_{0.5}MoO_4]\cdot 1.5H_2O$ (**3**·$1.5H_2O$). The structures of **1**–**3** exhibit three-dimensional covalent frameworks, constructed from bimetallic oxide layers tethered by the dipodal organoimine ligands. However, the $\{CuMoO_4\}$ networks are quite distinct. For structure **1**, the layer consists of corner-sharing $\{MoO_4\}$ tetrehedra and $\{CuN_2O_3\}$ square pyramids, while the layer of **2** is constructed from $\{MoO_4\}$ tetrehedra and binuclear $\{Cu_2O_6N_2\}$ units of edge-sharing copper square pyramids. The oxide substructure of **3** consists of $\{MoO_4\}$ tetrahedra corner-sharing with tetranuclear clusters of edge-sharing $\{CuO_5N\}$ octahedra. Crystal data: $C_{10}H_8N_2O_4CuMo$ **(1)**, orthorhombic *Pbca*, $a = 12.4823(6)$ Å, $b = 9.1699(4)$ Å, $c = 19.5647(9)$ Å, $V = 2239.4(1)$ Å$^3$, $Z = 8$; $C_5H_4NO_4CuMo$ **(2)**, triclinic $P\bar{1}$, $a = 5.439(1)$ Å, $b = 6.814(1)$ Å, $c = 10.727(2)$ Å, $\alpha = 73.909(4)^o$, $\beta = 78.839(4)^o$; $\gamma = 70.389(4)^o$; $V = 357.6(1)$ Å$^3$, $Z = 2$; $C_{10}H_8N_2O_8Cu_2Mo_2\cdot 3H_2O$ **3**·$1.5H_2O$, triclinic $P\bar{1}$, $a = 7.4273(7)$ Å, $b = 9.2314(8)$ Å, $c = 13.880(1)$ Å, $\alpha = 71.411(2)^o$, $\beta = 88.528(2)^o$, $\gamma = 73.650(2)^o$, $V = 863.4(1)$ Å$^3$, $Z = 2$. The magnetic properties of **1**–**3** arise solely from the presence of the Cu(II) sites, but reflect the structural differences within the bimetallic oxide layers. Compound **1** exhibits magnetic behavior consistent with ferromagnetic chains which couple antiferromagnetically at low temperature. Compound **2** exhibits strong antiferromagnetic dimeric interactions, with the magnetic susceptibility data consistent with the Bleaney–Bowers equation. Similarly, the magnetic susceptibility of **3** is dominated by antiferromagnetic interactions, which may be modeled as a linear $S = 1/2$ Heisenberg tetramer.

Metal oxides continue to receive widespread attention in contemporary solid-state chemistry in view of their applications to catalysis, separations, molecular electronics, energy storage, optical materials, ceramics, and even heavy construction.[1−4] Layered inorganic oxides constitute an important subclass of solids notable for their unique characteristic of allowing a wide variety of organic or inorganic chemistries to be performed in the interlamellar region. However, since the mechanisms relevant to the assembly of extended inorganic solids are not fully understood, the development of metal oxide chemistry remains significantly dependent on the synthesis of materials possessing novel structures and properties.[5]

One successful strategy for the discovery of new oxide materials exploits organic molecules or cations in the

* To whom correspondence should be addressed. E-mail (J.Z.): jazubiet@syr.edu.
[†] Syracuse University.
[‡] McMaster University.
[§] State University of New York at Binghamton.
[||] King's College.

(1) Cheetham, A. J. *Science* **1996**, *264*, 794 and references therein.
(2) Hartman, M.; Kevan, L. *Chem. Rev.* **1999**, *99*, 635.
(3) Cockayne, B., Jones, D. W., Eds. *Modern Oxide Materials*; Academic Press: New York, 1972.
(4) Büchner, W.; Schiebs, R.; Winter, G.; Büchel, K. H. *Industrial Inorganic Chemistry*; VCM: New York, 1989.
(5) Bhuvanesh, N. S. P.; Prasad, B. R.; Subramanian, C. K.; Gopalakrishnan, J. *Chem. Commun*. **1996**, 289.



10.1021/ic0111536 CCC: $22.00 
Published on Web 03/26/2002

preparation of organic/inorganic hybrid materials which may exhibit composite or new properties and often unique structures.[6] In the course of our investigations of vanadium oxide[7−13] and molybdenun oxide solids,[14−30] we have modified this approach by introducing a secondary transition-metal cation, as well as the organic component which functions as a ligand. In this fashion, the hybrid bimetallic oxide structures reflect not only the influences of the ligand, such as donor group geometry, tether length, steric constraints, ligation either to the secondary metal or to the vanadate or molybdate substructure, but also the coordination preferences of the secondary metal. This latter point is nicely illustrated by the contrasting structures of [Cu(terpy)$Mo_2O_7$] and [Zn(terpy)-$Mo_2O_7$].[31] The profound structural consequences associated with ligand geometry are likewise evident in the distinctive structures of [Cu(pyrazine)$_{0.5}MoO_4$] and [$Cu_2$(pyrimidine)-$Mo_3O_{10}$].[25]

It is also noteworthy that the M′/Mo/O/ligand family of bimetallic oxides is represented by two major classes of compounds, depending on the reaction conditions for synthesis: (1) solids exhibiting molybdate cluster anions and secondary metal/ligand complexes or polymeric cations as building blocks and (2) bimetallic oxide networks, buttressed or decorated by the organic component, that is, structures which do not exhibit a distinct molybate substructure; rather the molybdate subunit is embedded within the bimetallic oxide scaffolding. In the course of our investigations of the latter class of materials, it was noted that subtle changes in ligand geometry or donor group orientation could produce unanticipated structural consequences. To further explore this observation, the structural consequences of ligand modification in the series 4,4′-bipyridine (4,4′-bpy), 3,3′-bipyridine (3,3′-bpy), and 3,4′-bipyridine (3,4′-bpy) were studied for the copper molybdate family. Herein, we report the structures and magnetic properties of the bimetallic oxides [Cu(3,4′-bpy) $MoO_4$] **(1)**, [Cu(3,3′-bpy)$_{0.5}MoO_4$] **(2),** and [Cu(4,4′-bpy)$_{0.5}MoO_4$]·1.5$H_2O$ (**3**·1.5$H_2O$).

## Experimental Section

**General Considerations**.

Reagents were purchased from Aldrich Chemical Co. and used without further purification. All syntheses were carried out in 23 mL poly(tetrafluoroethylene)-lined stainless steel containers under autogenous pressure. The reactants were stirred briefly before heating. Water was distilled above 3.0 M Ω in-house using a Barnstead Model 525 Biopure Distilled Water Center.

**Synthesis of 3,3′-bpy**.

All manipulations were carried out under an atmosphere of dry nitrogen. Trimethyltin chloride (50 g) was dissolved in 50 mL of ethylene glycol dimethyl ether (dme). This solution was added dropwise with stirring over a period of 20 m to a solution of sodium (18 g) in dme (200 mL) in a 500 mL round-bottom flask in a salt/ice bath at −10 °C.

After 2 h of stirring, the solution turned dark green. The round-bottom flask was then transferred to a glovebox; the mixture was filtered through a course funnel and transferred to another 500 mL round-bottom flask. The 500 mL round-bottom flask was then taken from the glovebox and placed back on a Schlenk line. 3-Bromopyridine (20 g) dissolved in 150 mL of dme was added dropwise to the solution in an ice/salt bath and stirred for 3 h to yield a yellow solution. The solvent was then removed under vacuum at room temperature to produce a thick yellow paste. Ether (250 mL) was added to the paste, and the solution was filtered in a glovebox to remove the NaBr byproduct. The solution was then returned to the Schlenk line, whereupon ether was removed under vacuum to produce a yellow/orange paste, which was then distilled through a short-path distillation apparatus to yield two fractions. The second fraction of 3-(trimethylstannyl)pyridine, which distilled at 45 °C, was collected for further use.

The clear solution of 3-(trimethylstannyl)pyridine was refluxed for 12 h in freshly distilled xylene (1 L), containing tetrakis-(triphenylphosphine)palladium(0) (2.4 g) and 3-bromopyridine (30 g). The solution turned yellow upon mixing, and then dark green upon refluxing. After cooling, a dark green solid precipitated to leave a light yellow solution. The solution was extracted with 15% HCl. The aqueous layer was collected and extracted with ether (500 mL in 100 mL portions). The aqueous layer was collected and NaOH added to pH 8.0, whereupon the solution turned orange. The orange solution was washed with chloroform, dried over sodium sulfate, and gravity filtered. Solvent removal in vacuo yielded a yellow paste, which was eluted through an alumina column in ether.


(6) (a) Stupp, S. I.; Braun, P. V. *Science* **1997**, *277*, 1242. (b) Davis, M. E.; Katz, A.; Ahmad, W. R. *Chem. Mater.* **1996**, *8*, 1820.
(7) Zhang, Y.; DeBord, J. R. D.; O'Connor, C. J.; Haushalter, R. C.; Clearfield, A.; Zubieta, J. *Angew. Chem., Int. Ed. Engl.* **1996**, *35*, 989.
(8) DeBord, J. R. D.; Zhang, Y.; Haushalter, R. C.; Zubieta, J.; O'Connor, C. J. *J. Solid State Chem.* **1996**, *122*, 251.
(9) LaDuca, R. L., Jr.; Finn, R. C.; Zubieta, J. *Chem. Commun.* **1999**, 1669.
(10) LaDuca, R. L., Jr.; Rarig, R. S., Jr.; Zubieta, J. *Inorg. Chem.* **2001**, *40*.
(11) Ollivier, P. J.; DeBord, J. R. D.; Zapf, P. J.; Zubieta, J.; Meyer, L. M.; Wang, C.-C.; Mallouk, T. E.; Haushalter, R. C. *J. Mol. Struct.* **1998**, *470*, 49.
(12) Hagrman, P. J.; Bridges, C.; Greedan, J. E.; Zubieta, J. *J. Chem. Soc., Dalton Trans.* **1999**, 2901.
(13) LaDuca, R. C., Jr.; Brodkin, C.; Finn, R. C.; Zubieta, J. *Inorg. Chem. Commun.* **2000**, *3*, 248.
(14) Hagrman, P. J.; Hagrman, D.; Zubieta, J. *Angew. Chem., Int. Ed.* **1999**, *38*, 2638.
(15) Hagrman, D.; Zubieta, C.; Haushalter, R. C.; Zubieta, J. *Angew. Chem., Int. Ed. Engl.* **1997**, *36*, 873.
(16) Hagrman, D.; Sangregorio, C.; O'Connor, C. J.; Zubieta, J. *J. Chem. Soc., Dalton Trans.* **1998**, 3707.
(17) Hagrman, D.; Hagrman, P.; Zubieta, J. *Inorg. Chim. Acta* **2000**, *300*−*302*, 212.
(18) DeBord, J. R. D.; Haushalter, R. C.; Meyer, L. M.; Rose, D. J.; Zapf, P. J.; Zubieta, J. *Inorg. Chim. Acta* **1997**, *256*, 165.
(19) Hagrman, D.; Zapf, P. J.; Zubieta, J. *Chem. Commun.* **1998**, 1283.
(20) Hagrman, D.; Hagrman, P. J.; Zubieta, J. *Angew. Chem., Int. Ed.* **1999**, *38*, 3165.
(21) Hagrman, D.; Zubieta, J. *C. R. Acad. Sci., Ser. IIc: Chim.* **2000**, *3*, 231.
(22) Hagrman, D.; Hagrman, P. J.; Zubieta, J. *Comments Inorg. Chem.* **1999**, *21*, 225 and references therein.
(23) Chesnut, D. J.; Hagrman, D.; Zapf, P. J.; Hammond, R. P.; LaDuca, R., Jr.; Haushalter, R. C.; Zubieta, J. *Coord. Chem. Rev.* **1999**, *190*−*192*, 737.
(24) Zapf, P. J.; Hammond, R. P.; Haushalter, R. C.; Zubieta, J. *Chem. Mater.* **1998**, *10*, 1366.
(25) Hagrman, D.; Warren, C. J.; Haushalter, R. C.; Seip, C.; O'Connor, C. J.; Rarig, R. S., Jr.; Johnson, K. M., III; LaDuca, R. L., Jr.; Zubieta, J. *Chem. Mater.* **1998**, *10*, 3294.
(26) Hagrman, D.; Haushalter, R. C.; Zubieta, J. *Chem. Mater.* **1998**, *10*, 361.
(27) Laskoski, M. C.; LaDuca, R. L., Jr.; Rarig, R. S., Jr.; Zubieta, J. *J. Chem. Soc., Dalton, Trans.* **1999**, 3467.
(28) Hagrman, D. E.; Zubieta, J. *J. Solid State Chem.* **2000**, *152*, 141.
(29) LaDuca, R. L., Jr.; Desciak, M.; Laskoski, M.; Rarig, R. S., Jr.; Zubieta, J. *J. Chem. Soc., Dalton Trans.* **2000**, 2255.
(30) Zapf, P. J.; Warren, C. J.; Haushalter, R. C.; Zubieta, J. *Chem. Commun.* **1997**, 1543.
(31) Hagrman, P. J.; Zubieta, J. *Inorg. Chem.* **2000**, *39*, 5218.

The ether was removed in vacuo, and the resulting paste was distilled in a short-path distillation apparatus to yield the product at 98 °C.

**Synthesis of 3,4′-bpy**.

3,4′-bpy was prepared in a manner similar to that of 3,3′-bpy with the exception that 4-bromopyridine was used for the coupling reaction in place of 3-bromopyridine.

**Synthesis of 1**.

A mixture of $CuSO_4 \cdot 5H_2O$ (0.097 g, 0.39 mmol), $MoO_3$ (0.053 g, 0.37 mmol), 3,4′-bipyridine (0.058 g, 0.37 mmol), and $H_2O$ (10.0 g, 0.56 mol) in the mole ratio 1:1:1:1500 was heated at 120 °C for 72 h. Blue crystals of **1** were isolated in 85% yield based on Mo.

**Synthesis of 2**.

A mixture of $CuCl_2 \cdot 2H_2O$ (0.094 g, 0.54 mmol), $MoO_3$ (0.079 g, 0.54 mmol), 3,3′-bipyridine (0.07 g, 0.54 mmol), $H_2O$ (10.0 g, 0.56 mol), and sufficient 20% $(C_4H_9)_4NOH$ to adjust the pH to 7.2 was heated to 180 °C for 75 h, whereupon green crystals of **2** were isolated in 80% yield based on Mo.

**Synthesis of 3·1.5H$_2$O**.

A mixture of $CuCl_2 \cdot 2H_2O$ (0.038 g, 0.22 mmol), $MoO_3$ (0.032 g, 0.22 mmol), 4,4′-bipyridine (0.055 g, 0.22 mmol), and $H_2O$ (10.0 g, 0.56 mol) was heated at 120 °C for 214 h. Green crystals of **3**·1.5$H_2O$ were isolated in 20% yield based on Mo.

**X-ray Crystallography**.

Structural measurements for **1**−**3** were performed on a Bruker SMART-CCD diffractometer at a temperature of 90 ± 1 K using graphite-monochromated Mo Kα radiation ($\lambda$(Mo Kα) = 0.71073 Å). The data were corrected for Lorentz and polarization effects and absorption using SADABS.[32] The structures were solved by direct methods.[33] In all cases, all non-hydrogen atoms were refined anistropically. After all of the non-hydrogen atoms were located, the models were refined against $F^2$, initially using isotropic and later anisotropic thermal displacement parameters until the final values of $\Delta/\sigma_{max}$ were less than 0.001 in all cases. Hydrogen atoms were introduced in calculated positions and refined isotropically. Neutral atom scattering coefficients and anomalous dispersion corrections were taken from the *International Tables*, Vol. C. All calculations were performed using the SHELXTL[34] crystallographic software packages.

Crystallographic details for the structures of **1**−**3** are summarized in Table 1.

Atomic positional parameters, full tables of bond lengths and angles, and anisotropic temperature factors are available in the Supporting Information. Selected bond lengths and angles for **1**−**3** are given in Tables 2−4, respectively.

**Magnetic Measurements**.

Samples (10−30 mg) were placed in gelatin capsule holders and accurately weighed prior to data collection. Zero-field-cooled (ZFC) and field-cooled (FC) magnetic susceptibility data were collected on a Quantum Design SQUID magnetometer between 2 and 350 K with an applied field of 500 (**3**·1.5$H_2O$) or 1000 (**1** and **2**) Oe. Paramagnetic susceptibilities were obtained by subtracting the diamagnetic contributions from the raw magnetic susceptibility data using Pascal's constants in emu mol$^{-1}$ units ($-1.7 \times 10^{-4}$ (**1**), $-2.4 \times 10^{-4}$ (**2**), $-2.8 \times 10^{-4}$ (**3**)).[35]

(32) SADABS, Data Collection Software, Version 4.050, Siemens Analytical Instruments Inc., Madison, WI, 1996.
(33) SMART, Data Collection Software, Version 4.050, Siemens Analytical Instruments Inc., Madison, WI, 1996.
(34) Sheldrick, G. M. SHELXTL PC, Version 5.0, Siemens Analytical Instruments Inc., Madison, WI, 1994.
(35) *Theory and Applications of Molecular Diamagnetism*; Mulay, L. N., Boudreaux, E. A., Eds.; Wiley-Interscience Publishers: New York, 1976.

**Table 1.** Summary of Crystallographic Data for the Structures of **1**, **2**, and **3**·1.5$H_2O$

| | **1** | **2** | **3**·1.5$H_2O$ |
|---|---|---|---|
| empirical formula | $C_{10}H_8N_2O_4CuMo$ | $C_5H_4NO_4CuMo$ | $C_{10}H_{14}N_2O_{11}Cu_2Mo_2$ |
| fw | 379.62 | 301.57 | 657.19 |
| cryst syst | orthorhomlic | triclinic | triclinic |
| space group | Pbca | $P\bar{1}$ | $P\bar{1}$ |
| *a*, Å | 12.4823(6) | 5.439(1) | 7.4273(7) |
| *b*, Å | 9.1699(4) | 6.814(1) | 9.2314(8) |
| *c*, Å | 19.5647(9) | 10.727(2) | 13.880(1) |
| α, deg | 90.0 | 73.909(4) | 71.411(2) |
| *β*, deg | 90.0 | 78.839(4) | 88.528(2) |
| *γ*, deg | 90.0 | 70.389(4) | 73.650(2) |
| *V*, Å$^3$ | 2239.4(1) | 357.6(1) | 863.4(1) |
| Z | 8 | 2 | 2 |
| $D_{calcd}$, g cm$^{-3}$ | 2.025 | 2.801 | 2.528 |
| $\mu$, cm$^{-1}$ | 30.26 | 46.92 | 39.10 |
| no. of reflns | 2751 | 1621 | 4003 |
| R1[a] | 0.0447 | 0.0506 | 0.0783 |
| wR2[b] | 0.0706 | 0.1134 | 0.1424 |

[a] $R1 = \sum|F_o| - |F_c|/\sum|F_o|$; $wR2 = \{\sum[w(F_o^2 - F_c^2)^2]/\sum[w(F_o^2)^2]\}^{1/2}$.

**Table 2.** Bond Lengths (Å) and Angles (deg) for **1**[a]

| | | | |
|---|---|---|---|
| Cu(1)−O(1) | 1.939(2) | Mo(1)−O(4) | 1.730(2) |
| Cu(1)−O(3)#1 | 1.944(2) | Mo(1)−O(2) | 1.739(2) |
| Cu(1)−N(1) | 2.030(3) | Mo(1)−O(1) | 1.781(2) |
| Cu(1)−N(2) | 2.048(3) | Mo(1)−O(3) | 1.784(2) |
| Cu(1)−O(2)#2 | 2.213(2) | | |
| O(1)−Cu(1)−O(3)#1 | 172.8(1) | O(4)−Mo(1)−O(1) | 108.8(1) |
| O(1)−Cu(1)−N(1) | 91.0(1) | O(2)−Mo(1)−O(1) | 109.5(1) |
| O(3)#1−Cu(1)−N(1) | 87.1(1) | O(4)−Mo(1)−O(3) | 109.4(1) |
| O(1)−Cu(1)−N(2) | 90.5(1) | O(2)−Mo(1)−O(3) | 110.0(1) |
| O(3)#1−Cu(1)−N(2) | 89.39(1) | O(1)−Mo(1)−O(3) | 109.4(1) |
| N(1)−Cu(1)−N(2) | 163.9(1) | Mo(1)−O(1)−Cu(1) | 169.8(1) |
| O(1)−Cu(1)−O(2)#2 | 94.6(9) | Mo(1)−O(2)−Cu(1)#3 | 167.2(1) |
| O(3)#1−Cu(1)−O(2)#2 | 92.4(9) | Mo(1)−O(3)−Cu(1)#4 | 130.5(1) |
| N(1)−Cu(1)−O(2)#2 | 92.3(1) | C(10)−N(2)−Cu(1) | 120.2(2) |
| N(2)−Cu(1)−O(2)#2 | 103.5(1) | C(6)−N(2)−Cu(1) | 123.6(2) |
| O(4)−Mo(1)−O(2) | 109.8(1) | | |

[a] Symmetry transformations used to generate equivalent atoms: #1, $x - 1/2, y, -z + 1/2$; #2, $-x + 2, y - 1/2, -z + 1/2$; #3, $-x + 2, y + 1/2, -z + 1/2$; #4, $x + 1/2, y, -z + 1/2$; #5, $-x + 3/2, -y, z - 1/2$; #6, $-x + 3/2, -y, z + 1/2$.

**Table 3.** Selected Bond Lengths (Å) and Angles (deg) for **2**[a]

| | | | |
|---|---|---|---|
| Cu(1)−O(4)#1 | 1.944(4) | Mo(1)−O(1) | 1.713(4) |
| Cu(1)−O(2) | 1.964(4) | Mo(1)−O(3) | 1.733(4) |
| Cu(1)−O(2)#2 | 1.969(4) | Mo(1)−O(4) | 1.798(4) |
| Cu(1)−N(1) | 1.982(5) | Mo(1)−O(2) | 1.852(4) |
| Cu(1)−O(3))#3 | 2.174(4) | | |
| O(1)−Mo(1)−O(3) | 106.79(19) | O(2)−Cu(1)−N(1) | 94.06(17) |
| O(1)−Mo(1)−O(4) | 106.51(18) | O(2)#2−Cu(1)−N(1) | 165.05(19) |
| O(3)−Mo(1)−O(4) | 113.11(18) | O(4)#1−Cu(1)−O(3)#3 | 96.19(16) |
| O(1)−Mo(1)−O(2) | 105.64(18) | O(2)−Cu(1)−O(3)#3 | 96.35(16) |
| O(3)−Mo(1)−O(2) | 112.13(18) | O(2)#2−Cu(1)−O(3)#3 | 100.01(16) |
| O(4)−Mo(1)−O(2) | 112.07(18) | N(1)−Cu(1)−O(3)#3 | 94.72(17) |
| O(4)#1−Cu(1)−O(2) | 165.00(17) | Mo(1)−O(2)−Cu(1)#2 | 114.70(19) |
| O(4)#1−Cu(1)−O(2)#2 | 87.84(15) | Cu(1)−O(2)−Cu(1)#2 | 98.09(17) |
| O(2)−Cu(1)−O(2)#2 | 81.91(17) | Mo(1)−O(3)−Cu(1)#3 | 145.3(2) |
| O(4)#1−Cu(1)−N(1) | 93.07(17) | | |

[a] Symmetry transformations used to generate equivalent atoms: #1, $x, y - 1, z$; #2, $-x + 1, -y + 1, -z$; #3, $-x + 2, -y + 1, -z$; #4, $x, y + 1, z$; #5, $-x + 2, -y, -z + 1$.

## Results and Discussion

**Synthesis, Spectroscopy, and Structural Studies**.

The compounds of this study were prepared using conventional hydrothermal methods. Exploitation of hydrothermal techniques of synthesis allows the preservation of the structural integrity of the organic component, while also providing conditions which favor the isolation of metastable

**Table 4.** Bond Lengths (Å) and Angles (deg) for **3**·1.5$H_2O$

| | | | |
|---|---|---|---|
| Mo(1)−O(8) | 1.744(5) | Cu(1)−N(1) | 1.986(6) |
| Mo(1)−O(2) | 1.747(5) | Cu(1)−O(5)#1[a] | 2.014(5) |
| Mo(1)−O(7) | 1.780(5) | Cu(1)−O(5)#2 | 2.346(5) |
| Mo(1)−O(6) | 1.798(5) | Cu(1)−O(1) | 2.377(5) |
| Mo(2)−O(3) | 1.721(6) | Cu(2)−O(8)#3 | 1.949(5) |
| Mo(2)−O(5) | 1.786(5) | Cu(2)−O(4)#1 | 1.978(5) |
| Mo(2)−O(4) | 1.789(5) | Cu(2)−N(2) | 2.009(6) |
| Mo(2)−O(1) | 1.817(5) | Cu(2)−O(1) | 2.024(5) |
| Cu(1)−O(7)#1 | 1.962(5) | Cu(2)−O(2) | 2.269(5) |
| Cu(1)−O(6)#2 | 1.984(5) | | |
| O(8)−Mo(1)−O(2) | 108.1(2) | O(7)#1−Cu(1)−O(6)#2 | 171.0(2) |
| O(8)−Mo(1)−O(7) | 107.0(2) | O(7)#1−Cu(1)−N(1) | 93.1(2) |
| O(2)−Mo(1)−O(7) | 112.3(2) | O(6)#2−Cu(1)−N(1) | 93.7(2) |
| O(8)−Mo(1)−O(6) | 106.8(2) | O(7)#1−Cu(1)−O(5)#1 | 85.3(2) |
| O(2)−Mo(1)−O(6) | 109.9(2) | O(6)#2−Cu(1)−O(5)#1 | 87.9(2) |
| O(7)−Mo(1)−O(6) | 112.5(2) | N(1)−Cu(1)−O(5)#1 | 178.3(2) |
| O(3)−Mo(2)−O(5) | 107.3(2) | O(7)#1−Cu(1)−O(5)#2 | 90.0(2) |
| O(3)−Mo(2)−O(4) | 106.2(2) | O(6)#2−Cu(1)−O(5)#2 | 83.2(2) |
| O(5)−Mo(2)−O(4) | 112.1(2) | N(1)−Cu(1)−O(5)#2 | 96.9(2) |
| O(3)−Mo(2)−O(1) | 106.2(2) | O(5)#1−Cu(1)−O(5)#2 | 82.5(2) |
| O(5)−Mo(2)−O(1) | 111.3(2) | O(7)#1−Cu(1)−O(1) | 100.2(2) |
| O(4)−Mo(2)−O(1) | 113.2(2) | O(6)#2−Cu(1)−O(1) | 84.4(2) |

[a] Symmetry transformations used to generate equivalent atoms: #1, $-x+1, -y+2, z$; #2, $x+1, y, z$.

phases and which encourage crystal growth from solution.[36] In a representative synthesis, a mixture of $CuSO_4$·$5H_2O$, $MoO_3$, 3,4′-bipyridine, and $H_2O$ in the mole ratio 1.1:1.0:1.0:1500 was heated at 120 °C for 72 h to give blue crystals of **1** in 85% yield. While $CuSO_4$·$5H_2O$ could also be used as the Cu(II) source in the preparations of **2** and **3**, optimization studies indicated that improved yields were obtained with $CuCl_2$·$2H_2O$ as the starting material. It was likewise observed that raising the reaction temperature to 180 °C improved the yield and crystallinity in the case of compound **2**.

The infrared spectra of **1**−**3** exhibited a strong band in the 920−935 $cm^{-1}$ range attributed to $\nu$(Mo═O). Medium-intensity features in the 780−820 $cm^{-1}$ region are tentatively attributed to $\nu$(Cu−O−Mo). A series of six to eight medium-intensity bands in the 1000−1600 $cm^{-1}$ region are associated with the organodiimine ligands.

The thermal decomposition profile of **1** indicates that the material is stable to 250 °C, whereupon ligand loss occurs to give an amorphous residue (38% weight loss; 41.1% calculated for loss of ligand). Compound **2** is stable to 325 °C, whereupon a weight loss of ca. 26% occurs over a temperature range of 325−375 °C (25.9% calculated for loss of ligand). Compound **3** exhibits a dehydration process which begins almost immediately on heating, indicative of loosely held water of crystallization within the interlameller cavities. The weight loss of ca. 4% by 110 °C is consistent with loss of the water of crystallization (4.1%, calculated for 1.5$H_2O$ per [Cu(4,4′-bpy)$MoO_4$] unit). A second weight loss of 25% in the range 320−385 °C is attributed to ligand combustion.

As shown in Figure 1a, the structure of **1** consists of bimetallic {$CuMoO_4$} oxide layers covalently linked through 3,4′-bpy ligands into a three-dimensional framework. Thus, the structure exhibits the characteristic pattern of alternating organic/inorganic domains previously described for metal organophosphonate phases.[37]

The oxide layer, shown in Figure 1b, is constructed from corner-sharing {$MoO_4$} tetrahedra and {$CuN_2O_3$} square pyramids.[38] The coordination geometry at the Cu(II) sites is defined by two nitrogen donors from two 3,4′-bpy ligands in the axial positions and three oxygen donors from the molybdate tetrahedra in the equatorial plane. Each 3,4′-bpy ligand tethers Cu(II) sites in adjacent layers to produce a one-dimensional $\{Cu(3,4'\text{-bpy})\}_n^{2n+}$ chain as a substructural component. Each $\{MoO_4\}^{2-}$ tetrahedron bridges three Cu(II) sites, leaving one terminal oxo group, which is directed into the interlamellar region. The covalent connectivity in the layer produces 12-membered {$Cu_3Mo_3O_6$} rings, which fuse to propagate the network structure.

The structure of **2** also exhibits the common pattern of alternating inorganic oxide networks and tethering organic ligand domains, as shown in Figure 2a. However, in contrast to the {$CuMoO_4$} network structure of **1**, the {$CuMoO_4$} network of **2** is constructed from molybdate tetrahedra and binuclear units of Cu(II) square pyramids, shown in Figure 2b. The geometry at each Cu(II) center is defined by an apical oxo group and three oxo groups and a nitrogen donor from the 3,3′-bpy ligand in the basal plane. Two Cu(II) sites share a basal (O−O) edge to form the binuclear unit. Since a given Cu(II) site coordinates to a single 3,3′-bpy ligand, the Cu(II)/ligand chains propagate as $\{Cu_2(3,3'\text{-bpy})\}_n^{4n+}$ chains, shown in Figure 2c, rather than the simple $\{Cu(3,4'\text{-bpy}\}_n^{2n+}$ chains of Figure 1c.

Each binuclear Cu(II) site is linked to six molybdate sites through corner-sharing to bridging oxo groups. Each $\{MoO_4\}^{2-}$ tetrahedron in turn bridges three binuclear copper sites, leaving one terminal oxo group to project into the interlamellar region. One consequence of the network connectivity is to generate eight-membered {$Cu_2Mo_2O_4$} rings. Adjacent "chains" of such fused rings are at right angles to each other to produce a ruffled bimetallic oxide layer.

The structure of **3**·1.5$H_2O$ also exhibits the pattern of inorganic oxide layers alternating with bridging ligand domains (Figure 3a). However, in contrast to both **1** and **2**, the bimetallic oxide network of **3**, shown in Figure 3b, is constructed from $\{MoO_4\}^{2-}$ tetrahedra and tetranuclear units of edge-sharing {$CuNO_5$} octahedra. The coordination geometry at each Cu(II) site is defined by a nitrogen donor from the 4,4′-bpy ligand and five oxo groups from five corner-sharing molybdate tetrahedra. The 4,4′-bpy ligands bridge adjacent layers and produce $\{Cu_4(4,4'\text{-bpy})_2\}_n^{8n+}$ chains as substructural motifs (Figure 3c), which contrast rather dramatically with the $\{Cu(3,4'\text{-bpy})\}_n^{2n+}$ and $\{Cu_2(3,3'\text{-bpy})\}_n^{4n+}$ chains of **1** and **2**. Each tetranuclear Cu(II) cluster is linked to 10 molybdate tetrahedra. There are two distinct molybdate sites. One provides three bridging oxo groups to the copper clusters and exhibits a terminal oxo group not involved in Mo−O−Cu bridging, while the second links to three copper sites of one cluster and two copper sites of the adjacent cluster, with all oxo groups employed in Mo−

(36) Gopalakrishnan, J. *Chem. Mater.* **1995**, *7*, 1265.
(37) Khan, M. I.; Zubieta, J. *Prog. Inorg. Chem.* **1995**, *34*, 1.
(38) Addison, A. W.; Rao, T. N.; Reedjik, K.; Rejn, J.; Verschoor, G. C. *J. Chem. Soc., Dalton Trans.* **1984**, 1349.

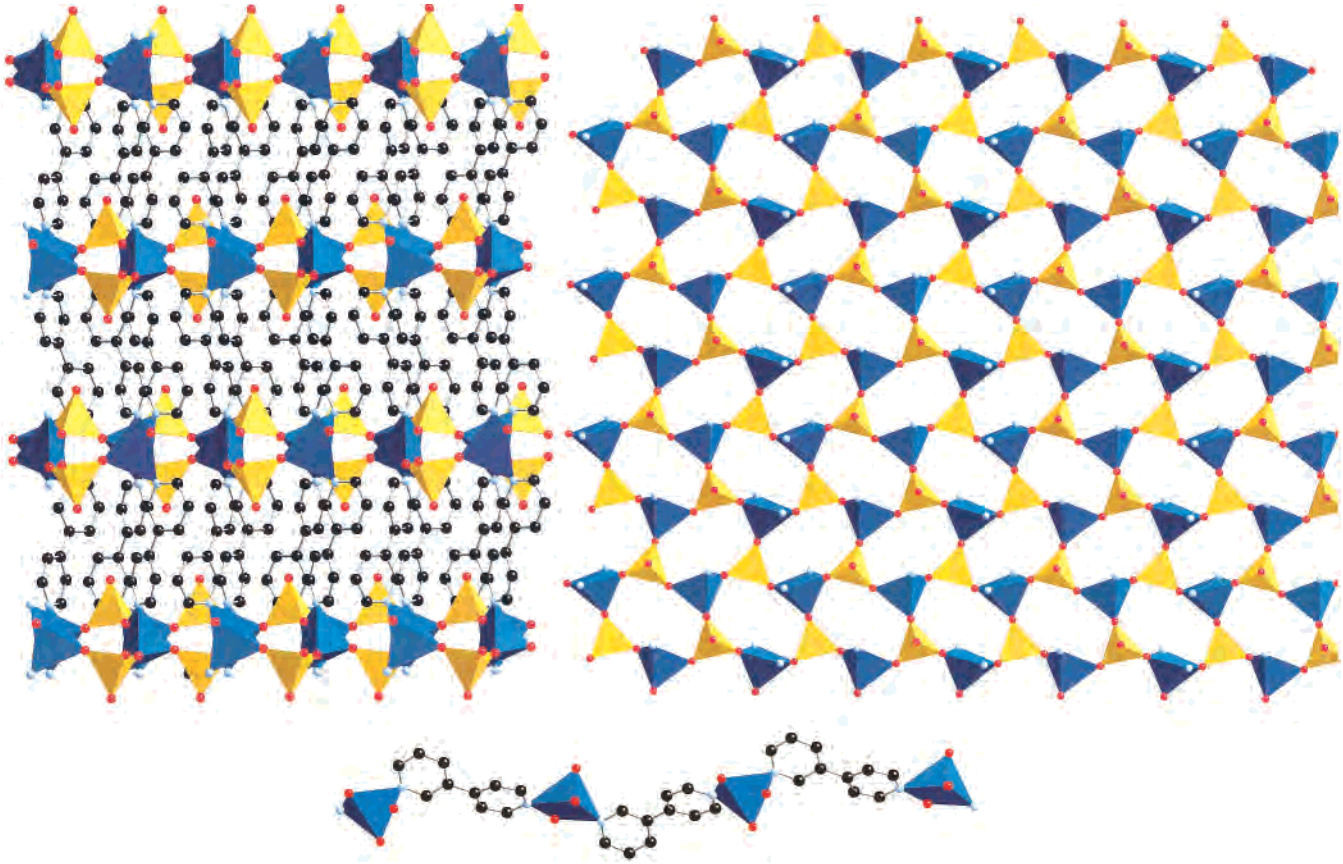

**Figure 1.** (a, top left) A view of the structure of **1**, parallel to the metal oxide planes, showing the alternating organic and inorganic domains. (b, top right) A polyhedral representation of the bimetallic oxide layer **1**. (c, bottom) Copper/ligand $\{Cu(3,4'\text{-bpy}\}_n^{2n+}$ chain crossing through the layers of **1**. The following color scheme has been adopted throughout: copper, blue polyhedra; molybdenum, yellow tetrahedra; oxygen, red spheres; carbon, black spheres; nitrogen, light blue spheres.

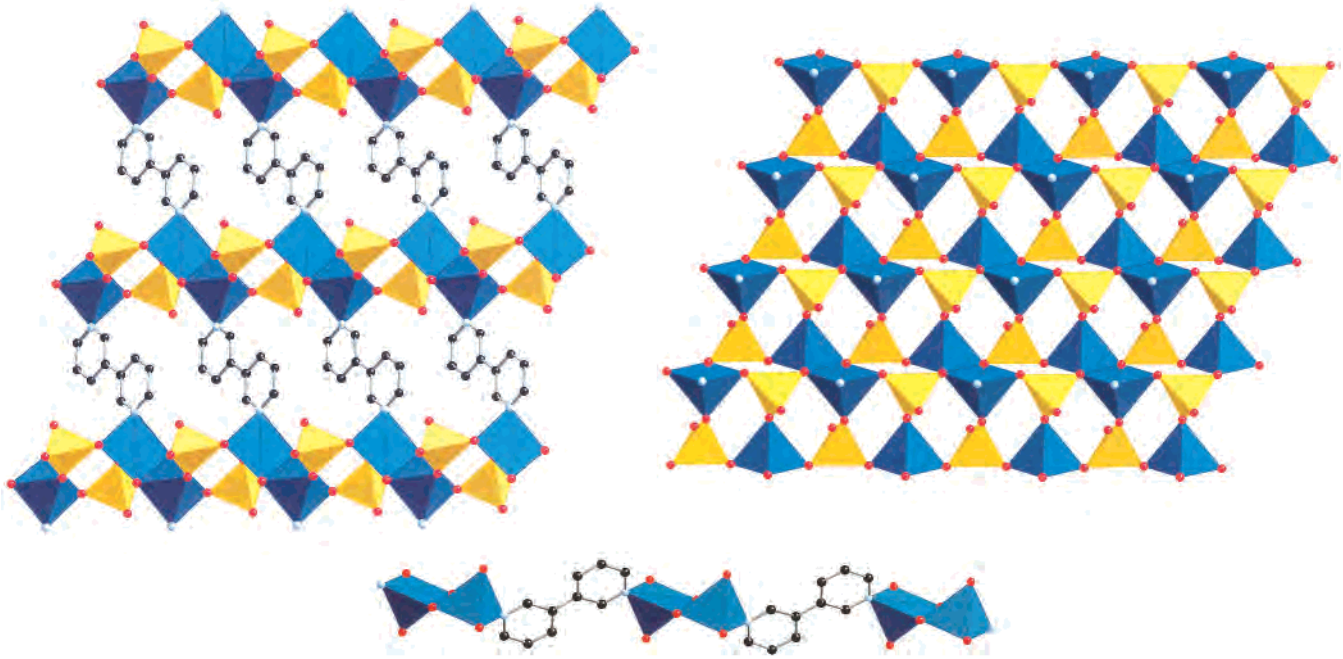

**Figure 2.** (a, top left) A view of the structure of **2**, parallel to the bimetallic oxide planes. (b, top right) A polyhedral representation of the metal oxide network of **2**. (c, bottom) Copper/ligand chain $\{Cu_2(3,3'\text{-bpy})\}_n^{4n+}$ crossing through the layers of **2**.

O−Cu bridging interactions. Consequently, in contrast to the structures of **1** and **2**, which exhibit only $\mu^2$-oxo groups {Cu−O−Mo}, the structure of **3** also possesses $\mu^3$-oxo groups $\{Cu_2MoO\}$. This more complex connectivity generates six-membered $\{Cu_2MoO_3\}$ rings as well as eight-membered $\{Cu_2Mo_2O_4\}$ rings as structural motifs of the oxide networks.

The structures of **1**−**3** clearly demonstrate the profound structural consequences which arise upon changes in the

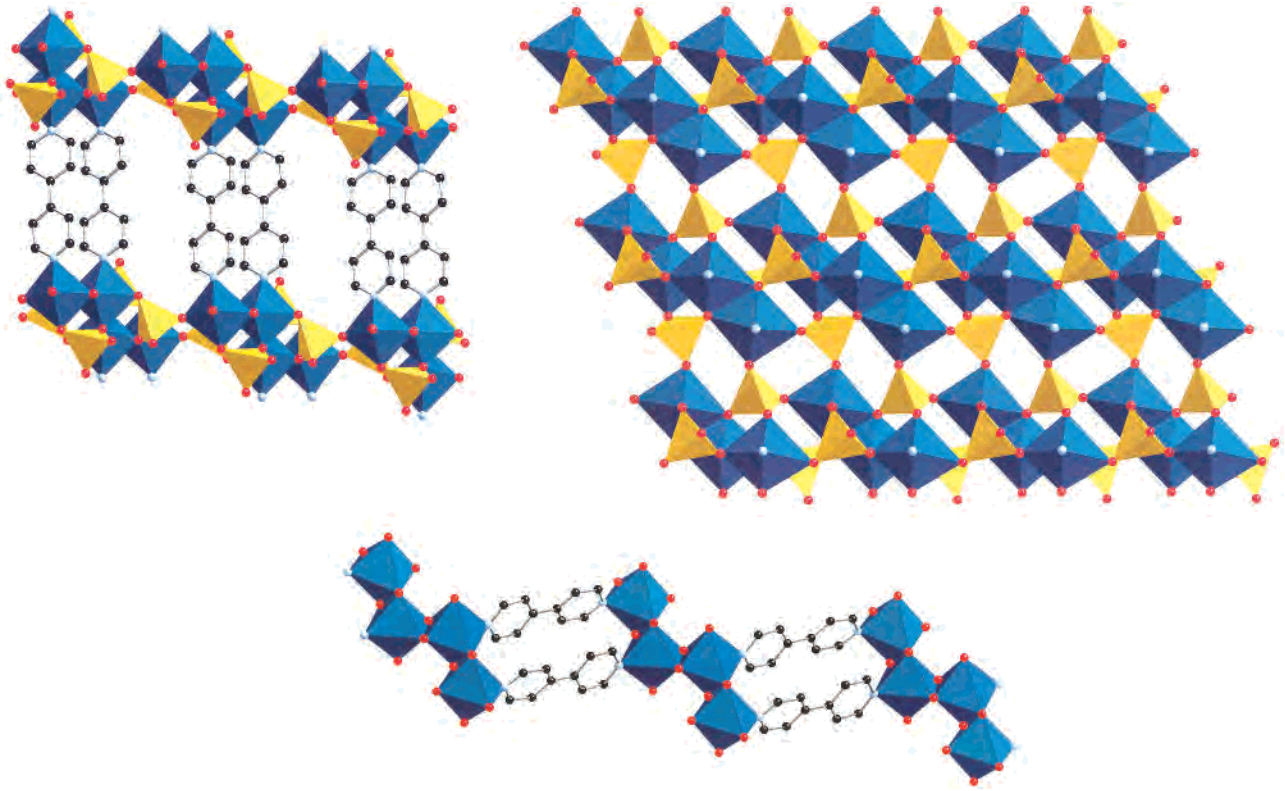

**Figure 3.** (a, top left) A view of the structure of **3**·1.5$H_2O$ parallel to the metal oxide planes. (b, top right) A polyhedral representation of the bimetallic oxide network of **3**. (c, bottom) One-dimensional $\{Cu_4(4,4'\text{-bpy})_n\}_n^{8n+}$ chains of **3**.

**Table 5.** Comparison of Structural Characteristics of Copper Molybdates with Dipodal Organodiimine Ligands Tethering Bimetallic Oxide Networks

| | interlamellar distance, Å | N···N distance of the ligand, Å | ligand/layer angle (deg)[a] |
|---|---|---|---|
| $[Cu(3,4'\text{-bpy})MoO_4]$ | 6.5 | 6.52 | 76.1 |
| $[Cu(3,3'\text{-bpy})_{0.5}MoO_4]$ | 5.9 | 6.16 | 52.0 |
| $[Cu(4,4'\text{-bpy})_{0.5}MoO_4]\cdot 1.5H_2O$ | 7.2 | 7.10 | 85.6 |
| $[Cu(dpe)MoO_4]$[b] | 12.2 | 9.39 | 81.5 |
| $[Cu(dpa)_{0.5}MoO_4]$[c] | 12.1 | 8.62 | 80.3 |

[a] The angle between the N···N vector of the ligand and the $\{CuMoO_4\}$ plane. [b] Reference 26. [c] Reference 25.

ligand geometry, such as donor group orientations in the series 3,3′-bpy, 3,4′-bpy, and 4,4′-bpy. The nature of the structural determinant is, however, not readily apparent. Thus, $[Cu(dpe)MoO_4]$[26] (dpe = 1,2-*trans*-(4,4′-dipyridyl)ethene) is structurally analogous to **1**, while $[Cu(dpa)_{0.5}MoO_4]$[25] (dpa = 4,4′-dipyridylamine) resembles **3**. Examining various gross structural parameters, we find, for example, that the interlayer spacings for **1**−**3** are ca. 6.5, 5.9, and 7.2 Å, respectively, while $[Cu(dpe)MoO_4]$ and $[Cu(dpa)_{0.5}MoO_4]$ exhibit spacings of 12.2 and 12.1 Å, respectively. The interlayer spacings reflect the introduction of additional atoms in the ligand tether and offer no structural correlation. Similarly, the ligand N···N distances and the approximate angle between the ligand N···N vector and the copper−molybdenum oxide planes, summarized in Table 5, reflect ligand geometric constraints, rather than the nuclearity of the copper subunit of the layer.

Just as the ligand geometry may dramatically modify the oxide microstructure, so too may the coordination preference of the secondary metal component. For example, the simple expedient of reducing the copper site to Cu(I) in the M′/Mo′/O/4,4′-bpy materials results in a structure based on octamolybdate clusters embedded in a lattice work of one-dimensional $\{Cu(4,4'\text{-bpy})\}_n^{n+}$ chains in $[\{Cu(4,4'\text{-bpy})\}_4Mo_8O_{26}]$ and, under modified reaction conditions, a structure constructed from one-dimensional $\{Mo_{15}O_{42}\}_n^{4n-}$ ribbons and $\{Cu(4,4'\text{-bpy})\}_n^{n+}$ chains in $[\{Cu(4,4'\text{-bpy})\}_4Mo_{15}O_{47}]$.[15] Of course, the major structural consequences manifested by reduction of the copper sites are not unexpected. Cu(II) coordination geometries reflect the Jahn−Teller distorted $d^9$ electronic configuration in square-planar and "4 + 1" or "4 + 2" environments. In contrast, Cu(I) in the presence of organoimine ligands adopts diagonal coordination or a "T"-shaped $\{CuN_2O\}$ or distorted tetrahedral $\{CuN_2O_2\}$ geometry upon expansion of the coordination sphere. Such grossly different coordination geometries at the copper sites result in significantly different Cu/ligand cationic substructures, which are reflected in the oxide architectures.

Similarly, the use of Ni(II) as the secondary metal introduces a component exhibiting more regular six coordination than that observed for the Jahn−Teller distorted Cu(II). Consequently, the structures of the dipodal bipyridine derivatives of the Ni(II)/molybdate family, $[\{Ni(3,3'\text{-bpy})_2\}_2Mo_4O_{14}]$,[39] $[Ni(3,4'\text{-bpy})_2MoO_4]$,[40] and $[Ni(H_2O)_2(4,4'\text{-bpy})_2\}_2Mo_8O_{26}]$,[15] are unrelated to the Cu(II)/molybdate materials of this study. Thus, $[Ni(3,4'\text{-bpy})_2MoO_4]$ consists of a three-dimensional $\{Ni(3,4'\text{-bpy})_2\}_n^{2n+}$ framework with

(39) LaDuca, R. L., Jr.; Desciak, M.; Laskoski, M.; Rarig, R. S., Jr.; Zubieta, J. *J. Chem. Soc., Dalton Trans.* **2000**, 2255.
(40) LaDuca, R. L., Jr.; Rarig, R. S., Jr.; Zubieta, J. Unpublished results.

entrained $\{MoO_4\}^{2-}$ tetrahedra. The $[\{Ni(3,3'\text{-bpy})_2\}_2Mo_4O_{14}]$ phase is two-dimensional, with $\{Mo_4O_{14}\}^{4-}$ clusters embedded in $\{Ni(3,4'\text{-bpy})_2\}_n^{2n+}$ sheets. The final example of the nickel molybdates $[\{Ni(H_2O)_2(4,4'\text{-bpy}\}_{22}Mo_8O_{26}]$ is also two-dimensional and constructed from $\{Mo_8O_{26}\}^{4-}$ clusters linked through $\{Ni(H_2O)_2(4,4'\text{-bpy})_2\}_n^{2n+}$ chains. Of course, such unique structural characteristics both within the Ni(II)/molybdate/ligand family and in comparison to the Cu(II)/molybdate/ligand family were unpredictable in detail.

**Magnetic Properties.**

Organic/inorganic hybrid materials provide new opportunities in the realm of molecular magnetism for studying magnetically condensed (i.e., exchange-coupled) systems.[41−43] Our ongoing investigations of vanadium oxide and molybdenum oxide solids, in which a secondary transition-metal cation is introduced, have shown that the resulting structures are influenced not only by the coordination preferences of the secondary metal but also by the characteristics of the organic ligand. In light of the magnetic properties of these materials, low-dimensional arrangements of the magnetic ions may be achieved through the use of nonmagnetic dividers such as fully oxidized metal ions or bulky organic substrates. For the compounds of this study, subtle changes in the donor group orientation of the organodiimine ligand result in a different description of the structure and magnetism of the paramagnetic metal centers within the two-dimensional bimetallic oxide layers.

The magnetism of **1**−**3** may be attributed solely to the presence of $Cu^{2+}$ ions ($3d^9$; $S = 1/2$) which reside in the $\{CuMoO_4\}$ layers in the three structures. Since $Mo^{6+}$ ($3d^0$; $S = 0$) ions do not possess an effective magnetic moment, they do not contribute to the bulk properties. The magnetism is further simplified by the fact that the bimetallic oxide layers are insulated from one another owing to the bulky organodiimine ligands filling the interlayer region in the solid state. As a result, Cu−Cu distances *between* the layers are greater than 9 Å in the three structures, precluding the possibility of significant interlayer exchange interactions. Thus, the magnetic properties of **1**−**3** may be adequately described by theories for low-dimensional cooperative phenomena. Figures 4−9 show the results of the magnetic measurements for all three compounds. The high-temperature region of the susceptibility data for **1** (300−350 K) and **2** (200−350 K) was fitted to the Curie−Weiss law, $\chi = C/T - \Theta$, where $C$ is the Curie constant, $T$ the temperature, and $\Theta$ the Weiss constant. Results for **1** ($C = 0.309(1)$ (emu K)/$mol_{Cu}$; $\Theta = 12(1)$ K) suggest ferromagnetic correlations, as indicated by the positive Weiss constant. The behavior of **2** ($C = 0.347(1)$ (emu K)/$mol_{Cu}$; $\Theta = -3.6(5)$ K) is dominated by antiferromagnetic interactions of the $Cu^{2+}$ ions. Surprisingly, the values of the Curie constant for compounds **1** and **2** are slightly smaller than expected. Unfortunately, a Curie−Weiss regime was not found in the susceptibility data for compound **3** even up to 350 K.

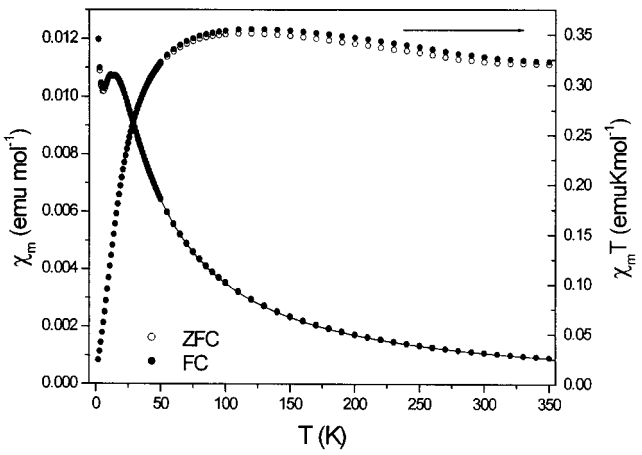


**Figure 4.** Temperature dependence of $\chi_m$ and $\chi_m T$ for **1** between 2 and 350 K. The light and dark circles represent ZFC and FC data, respectively. The solid line corresponds to the fit to the Baker model including a molecular field correction.

Figure 4 shows the temperature dependence of the molar susceptibility as well as the $\chi_m T$ product for **1**. A broad maximum is apparent in the $\chi_m$ vs $T$ plot at 13 K, indicative of antiferromagnetic ordering of the copper ions in the bimetallic oxide layers. Furthermore, the $\chi_m T$ vs $T$ plot provides evidence for additional ferromagnetic correlations above the Néel temperature, as there is a gradual increase with decreasing temperature followed by a rapid drop marking the onset of antiferromagnetic coupling. To explore possible pathways for these competing interactions, we examine more closely the construction of the two-dimensional layers in **1**. As mentioned previously, the $\{CuMoO_4\}$ slabs consist of corner-sharing $\{MoO_4\}$ tetrahedra and $\{CuN_2O_3\}$ square pyramids which alternate along the crystallographic *a* and *b* directions. An inspection of the intralayer Cu−Cu distances reveals that these are "short" (4.996(3) Å) as well as "long" (∼6.25 Å). The short distances occur along zigzag chains of alternating Cu square pyramids and Mo tetrahedra which run along *b* within the bimetallic oxide layer (pathway B). Continuing with this fragmented view of the layer, the ∼6.25 Å distances then represent the "interchain" separations. Alternatively, one may envisage copper chains extending along *a* with interchain interactions occurring along *b* (pathway A). It has been suggested that ferromagnetism can arise in carboxylato-bridged copper(II) complexes where the carboxylato adopts the anti−syn bridging mode and the Cu−O−C−O−Cu skeleton deviates from planarity.[44,45] It is not entirely obvious in the present case which pathway favors ferromagnetically coupled copper chains since on the basis of bond distance arguments, pathway B is favored, but on the basis of the deviation from planarity of the Cu−O−Mo−O−Cu superexchange pathway, pathway A is favored. Given the inequivalence of the two orthogonal superexchange pathways and the inability to assign, unambiguously, the sign of the exchange constants

(41) Drillon, M.; Panissod, P. *J. Magn. Magn. Mater.* **1998**, *188*, 93.
(42) Hornick, C.; Rabu, P.; Dillon, M. *Polyhedron* **2000**, *19*, 259.
(43) Finn, R. C.; Lam, R.; Greedan, J. E.; Zubieta, J. *Inorg. Chem.* **2001**, *40*, 3745.
(44) Ruiz-Pérez, C.; Sanchiz, J.; Molina, M. H.; Lloret, F.; Julve, M. *Inorg. Chem.* **2000**, *39*, 1363.
(45) Rodriguez-Martin, Y.; Ruiz-Pérez, C.; Sanchiz, J.; Lloret, F.; Julve, M. *Inorg. Chim. Acta* **2001**, *318*, 159.

along each, we can only suggest that one pathway gives rise to ferromagnetic chains and the other to antiferromagnetic interactions (interchain). Accordingly, the magnetic behavior of **1** appears to be consistent with ferromagnetic chains which couple antiferromagnetically at low temperature.

To determine the relative magnitude and sign of the exchange interactions, the magnetic susceptibility data above 40 K were fit to a linear chain model (Baker equation[46,47] for ferromagnetic Heisenberg chains of $S = 1/2$ centers) (eqs 1−4) including a molecular field correction[46,47] (eq 5)

$$\chi_{1D} \approx \frac{Ng^2\mu_B{}^2}{4kT}\left[\frac{P(y)}{Q(y)}\right]^{2/3} \quad (1)$$

$$P(y) = 1.0 + 5.7979916y + 16.902653y^2 + 29.376885y^3 + 29.832959y^4 + 14.036918y^5 \quad (2)$$

$$Q(y) = 1.0 + 2.7979916y + 7.0086780y^2 + 8.653644y^3 + 4.5743114y^4 \quad (3)$$

$$y = J/2kT \quad (4)$$

$$\chi_{2D} = \frac{\chi_{1D}}{1 - \chi_{1D}(2zJ'/Ng^2\mu_B{}^2)} \quad (5)$$

to account for antiferromagnetic interactions occurring between the chains. The magnetic constants and parameters have their usual meanings; $z$ is the number of nearest-neighbor chains (two in this case), $J$ the intrachain exchange constant, and $J'$ the interchain interaction. The final form of the magnetic susceptibility used in the fitting also included a term for the temperature-independent paramagnetism (TIP) of the sample: $\chi = \chi_{2D} + \text{TIP}$. The best fit (solid line in Figure 4) yielded $J/k = 37(1)$ K, $J'/k = -24.9(1)$ K, and $g = 1.958(8)$ (TIP $= -1.50(7) \times 10^{-4}$ emu/mol). The value for $g$ is slightly less than what is normally expected for $Cu^{2+}$ ions but is consistent with the Curie−Weiss fit. As a check on the consistency of the fitting procedure, one can calculate the Weiss constant given that the exchange constants are known, from the equation $\Theta_c = (2/3)S(S + 1)\sum(z_iJ_i/k)$.[48] Reassuringly, the calculated value of $\Theta_c$ (12 K), using $z = 2$ for both inter- and intrachain $J$ values, agrees with the one obtained directly from the Curie−Weiss fit ($\Theta = 12(1)$ K). The ferromagnetic exchange constant for **1** ($J/k = 37(1)$ K) may be compared to that of the malonato-bridged (Cu−O−C−O−Cu) compound $[Cu_2(mal)_2(H_2O)_2(4,4'\text{-bpy})]$ ($J/k = 18$ K).[45] As mentioned above, it is not clear what gives rise to the ferromagnetism observed in **1**. However, it is apparent that the two competing interactions are close in magnitude. At low temperature, the interchain antiferromagnetic correlations become important, dominating the overall magnetism. To determine whether **1** undergoes a metamagnetic transition, magnetization vs applied field experiments

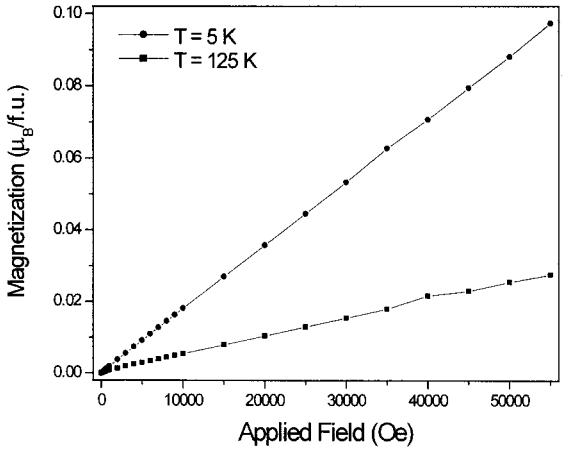


**Figure 5.** Magnetization vs applied field for **1** at $T = 5$ and 125 K.

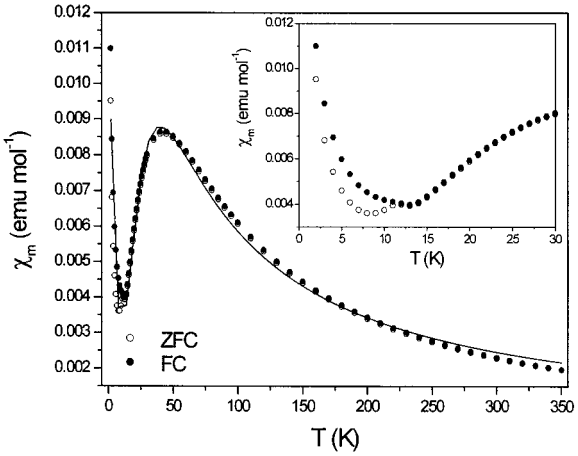


**Figure 6.** Temperature dependence of $\chi_m$ for **2** between 2 and 350 K. The inset shows an expanded view of the low-temperature region. The light and dark circles represent ZFC and FC data, respectively. The solid line corresponds to the fit to the Bleaney−Bowers model. The magnetic susceptibility is calculated per mole of copper dimer.

were performed at 5 and 125 K. As shown in Figure 5, the sample does not undergo such a transition up to 55000 Oe.

The magnetism of **2** should be more straightforward to interpret than that of **1** given that its bimetallic oxide layers are constructed from $\{MoO_4\}$ tetrahedra and binuclear clusters of edge-shared $Cu^{2+}$ square pyramids. The intra- and interdimer Cu−Cu distances are 2.970(3) and 5.521(3)−5.726(3) Å, respectively. Assuming that Cu−O−Cu exchange pathways within each cluster are more dominant than the Cu−O−Mo−O−Cu pathways between dimers, the magnetic properties of **2** are expected to resemble those of an isolated $S = 1/2$ dimer system. The temperature dependence of the molar susceptibility for **2** is shown in Figure 6, where a broad maximum is observed at 40 K, indicative of strong antiferromagnetic interactions. This is confirmed in Figure 7, where the $\chi_mT$ product clearly shows an antiferromagnetic ground state at low temperature. To determine the strength of the intradimer interaction, the magnetic susceptibility data were fitted to a modified Bleaney−Bowers equation[48,49] (eq 6) that takes into account the effects of

(46) Baker, G. A., Jr.; Rushbrooke, G. S.; Gilbert, H. E. *Phys. Rev.* **1964**, *135*, A1272.
(47) Deakin, L.; Arif, A. M.; Miller, J. S. *Inorg. Chem.* **1999**, *38*, 5072.
(48) *Magnetochemistry*; Carlin, R. L., Ed.; Springer-Verlag: New York, 1986.
(49) Bleaney, B.; Bowers, K. D. *Proc. R. Soc. London* **1952**, *A214*, 451.

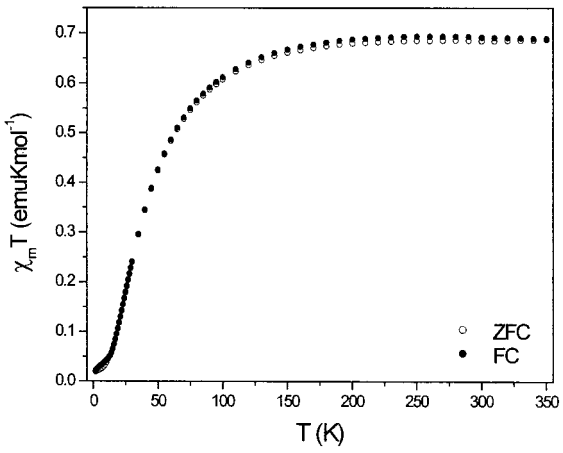


**Figure 7.** Temperature dependence of $\chi_m T$ for **2** between 2 and 350 K. The light and dark circles represent ZFC and FC data, respectively.

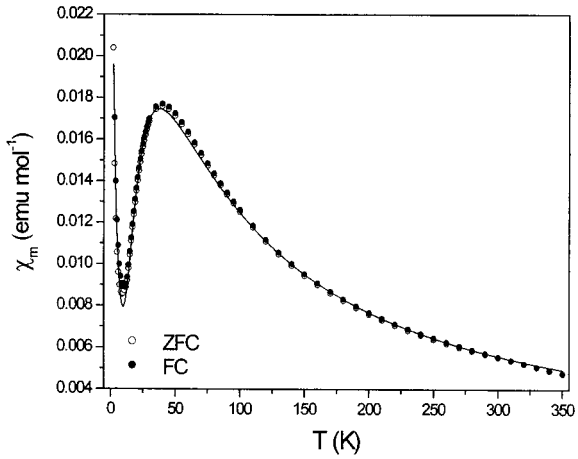


**Figure 8.** Temperature dependence of $\chi_m$ for **3** between 2 and 350 K. The light and dark circles represent ZFC and FC data, respectively. The solid line corresponds to the fit to the linear tetramer model. The magnetic susceptibility is calculated per mole of copper tetramer.

$$\chi_{\text{dimer}} = \frac{2Ng^2\mu_B{}^2}{3kT}\left[1 + \frac{1}{3}e^{-2J/kT}\right]^{-1} + \frac{C}{T-\Theta} + \text{TIP} \quad (6)$$

paramagnetic impurities and TIP. The best fit (solid line in Figure 6) resulted in the parameters $J/k = -33.8(3)$ K and $g = 1.86(2)$ (TIP $= 3.2(9) \times 10^{-4}$ emu/mol). Although the $g$ factor is less than expected for copper, it is consistent with the Curie constant obtained from the Curie−Weiss fit. Interestingly, an examination of the low-temperature region suggests long-range magnetic ordering below 12 K as indicated by the divergence in the ZFC/FC data. This may be attributed to the onset of interdimer antiferromagnetic coupling with possible complex field-dependent behavior.

Reminiscent of **2**, the structure of **3** shows that the bimetallic oxide layers consist of $\{MoO_4\}$ tetrahedra in addition to distinct clusters of $Cu^{2+}$ polyhedra, exemplified here by the tetranuclear units of edge-sharing $\{CuNO_5\}$ octahedra. Each tetramer is defined by outer Cu−Cu distances of 3.314(3) Å and an inner distance of 3.285(3) Å. These may be compared to intertetramer Cu−Cu separations of 4.943(3)−5.551(3) Å. Assuming that the former interactions are much stronger than the latter, the magnetic susceptibility of **3** may be approximated by a linear tetramer

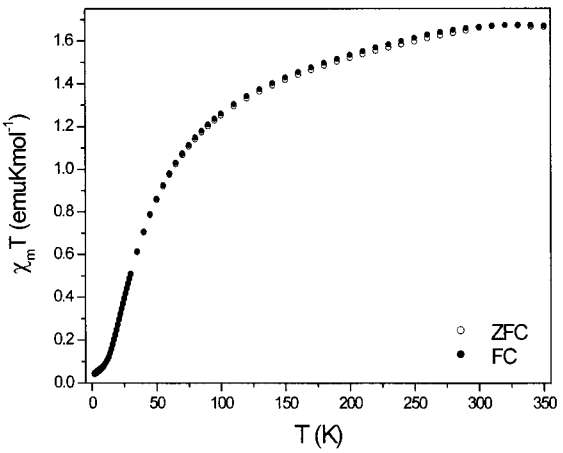


**Figure 9.** Temperature dependence of $\chi_m T$ for **3** between 2 and 350 K. The light and dark circles represent ZFC and FC data, respectively.

model. The magnetic susceptibility of **3** is shown in Figure 8, which displays a broad maximum at 40 K indicative of dominant antiferromagnetic interactions. Figure 9 shows a gradual decrease in the $\chi_m T$ product with decreasing temperature, which then drops rapidly at low temperature, a sure signature of an antiferromagnetic ground state. The Hamiltonian for a linear $S = 1/2$ Heisenberg tetramer, assuming only nearest-neighbor interactions, is $\mathbf{H} = -2J_a(\mathbf{S}_1\mathbf{S}_2 + \mathbf{S}_3\mathbf{S}_4) - 2J_b\mathbf{S}_2\mathbf{S}_3$, where $J_a$ and $J_b$ represent the exchange interactions between outer−inner and inner−inner atoms, respectively.[50,51] A best fit to the linear tetramer model (eqs 7−13),

$$\chi_{\text{tetramer}} = \frac{2Ng^2\mu_B{}^2}{kT}\left[\frac{10e^{-E_1/kT} + 2e^{-E_2/kT} + 2e^{-E_3/kT} + 2e^{-E_4/kT}}{5e^{-E_1/kT} + 3e^{-E_2/kT} + 3e^{-E_3/kT} + 3e^{-E_4/kT} + e^{-E_5/kT} + e^{-E_6/kT}}\right] \quad (7)$$

$$E_1 = -J_1 - 1/2J_2 \quad (8)$$

$$E_2 = J_1 - 1/2J_2 \quad (9)$$

$$E_3 = 1/2J_2 + (J_1{}^2 + J_2{}^2)^{1/2} \quad (10)$$

$$E_4 = 1/2J_2 - (J_1{}^2 + J_2{}^2)^{1/2} \quad (11)$$

$$E_5 = J_1 + 1/2J_2 + (4J_1{}^2 - 2J_1J_2 + J_2{}^2)^{1/2} \quad (12)$$

$$E_5 = J_1 + 1/2J_2 - (4J_1{}^2 - 2J_1J_2 + J_2{}^2)^{1/2} \quad (13)$$

modified to include terms for paramagnetic impurities and temperature-independent paramagnetism ($\chi_{\text{corrected}} = \chi_{\text{tetramer}} + C/(T - \Theta) + \text{TIP}$), yielded $J_a/k = -47(3)$ K, $J_b/k = -59(9)$ K, and $g = 2.02(5)$ (TIP $= 7(3) \times 10^{-4}$ emu/mol).

(50) Rubenacker, G. V.; Drumheller, J. E.; Emerson, K.; Willett, R. D. *J. Magn. Magn. Mater.* **1986**, *54*−*57*, 1483.
(51) Ayllón, J. A.; Santos, I. C.; Henriques, R. T.; Almeida, M.; Alcácer, L.; Duarte, M. T. *Inorg. Chem.* **1996**, *35*, 168.

The fact that $J_a \approx J_b$ is consistent with similar nearest-neighbor Cu−Cu distances in the tetramer.

## Conclusions

Hydrothermal methods have been exploited to prepare a new series of organic/inorganic hybrid materials of the oxomolybdenum/copper(II)/organoimine family. The compounds **1**, **2**, and **3**·1.5$H_2O$ exhibit three-dimensional covalently linked structures, constructed from bimetallic oxide layers buttressed by the organodiimine ligands. While the oxide layers of all three structures exhibit isolated $\{MoO_4\}^{2-}$ tetrahedra as building blocks, i.e., no Mo−O−Mo linkages, the copper constituents are distinct in each case: isolated $\{CuO_3N_2\}$ square pyramids in **1**, binuclear units of edge-sharing square pyramids in **2**, and tetranuclear clusters of edge-sharing octahedra in **3**. The materials exhibit magnetic properties arising from the presence of Cu(II) centers but reflecting the structural differences within the bimetallic oxide layers. The organic/inorganic hybrid materials **1**−**3** are examples of the design of structures with low-dimensional arrangements of magnetic ions, achieved through the introduction of nonmagnetic dividers, in these instances fully oxidized metals and bulky organic tethers.

**Acknowledgment.** This work was supported by a grant from the National Science Foundation (CHE9987471) and by a Research Grant (J.E.G.) from the National Sciences and Engineering Research Council of Canada.

**Supporting Information Available:** ORTEP figures of **1**−**3**, showing the atom-labeling schemes and 50% thermal ellipsoids, and three X-ray crystallographic files in CIF format. This material is available free of charge via the Internet at http://pubs.acs.org.

IC0111536